scientific reports

Check for updates

OPEN

Giant and highly anisotropic magnetocaloric effects in single crystals of disordered-perovskite $RCr_{0.5}Fe_{0.5}O_3$ (R = Gd, Er)

Hyun Jun Shin, Jin Seok Kim, Ki Won Jeong, Jong Hyuk Kim, Nara Lee✉ & Young Jai Choi✉

Magnetic anisotropy is crucial in examining suitable materials for magnetic functionalities because it affects their magnetic characteristics. In this study, disordered-perovskite $RCr_{0.5}Fe_{0.5}O_3$ (R = Gd, Er) single crystals were synthesized and the influence of magnetic anisotropy and additional ordering of rare-earth moments on cryogenic magnetocaloric properties was investigated. Both $GdCr_{0.5}Fe_{0.5}O_3$ (GCFO) and $ErCr_{0.5}Fe_{0.5}O_3$ (ECFO) crystallize in an orthorhombic *Pbnm* structure with randomly distributed Cr^{3+} and Fe^{3+} ions. In GCFO, the long-range order of Gd^{3+} moments emerges at a temperature of T_{Gd} (the ordering temperature of Gd^{3+} moments) = 12 K. The relatively isotropic nature of large Gd^{3+} moment originating from zero orbital angular momentum exhibits giant and virtually isotropic magnetocaloric effect (MCE), with a maximum magnetic entropy change of $\Delta S_M \approx 50.0$ J/kg·K. In ECFO, the highly anisotropic magnetizations result in a large rotating MCE characterized by a rotating magnetic entropy change $\Delta S_\theta = 20.8$ J/kg·K. These results indicate that a detailed understanding of magnetically anisotropic characteristics is the key for exploring improved functional properties in disordered perovskite oxides.

Increased popularity of energy-efficient magnetic refrigeration in clean technology has inspired extensive research on novel magnetic materials to discover an effective technique of enhancing the magnetocaloric effect (MCE), which is described as the variation of temperature (T) in a magnetic material by applying the magnetic field (H)[1–4]. The MCE can be estimated by an adiabatic T change (ΔT_{ad}) and an isothermal magnetic entropy change (ΔS_M) under the influence of H. Cryogenic magnetic refrigeration is crucial for obtaining sub-Kelvin temperatures as a substitute for ^{3}He/^{4}He dilution refrigeration despite of increased cost and hydrogen gas liquefaction, which is utilized as an alternative fuel. Recently, large cryogenic MCE has been discovered in various insulating transition-metal oxides[5–7] that possess easy manufacturability, chemical stability, and avoidance of refrigeration inefficiency because of eddy current. The beneficial aspect of MCE has been attained by the ΔT_{ad} in various oxide magnets, such as Gd_2CoMnO_6[8] (ΔT_{ad} = 1.3 K for ΔH = 0–9 T at 2 K and ΔT_{ad} = 8.3 K for ΔH = 0–9 T at 17 K), $SrFe_{0.5}Co_{0.5}O_3$[9] (ΔT_{ad} = 1.8 K for ΔH = 0–5 T at 330 K), $HoMnO_3$[10] (ΔT_{ad} = 10.8 K for ΔH = 0–7 T at 11 K), CrO_2[11] (ΔT_{ad} = 2.0 K for ΔH = 0–1.5 T at 390 K). Alternatively, the feasibility of magnetic refrigeration can be improved by developing a rotating MCE[8,12,13], which can be achieved by rotating the refrigerant at constant H. The advantages of this method are technical simplicity and device compactness. However, strong magnetic anisotropy is essential for the realization of refrigerant cooling, which can be achieved using single-crystalline magnets whose intrinsic magnetocrystalline anisotropy originates from the anisotropic spin–orbit interaction that varies with the symmetry and structure. Cryogenic rotating MCE has been observed in several insulating oxide magnets, such as $TbMnO_3$[14] (the magnetic entropy change obtained by rotation, ΔS_θ = 9.0 J/kg·K for 5 T at 15 K), $HoMn_2O_5$[15] (ΔS_θ = 12.4 J/kg·K for 7 T at 10 K), $TmFeO_3$[16] (ΔS_θ = 9.0 J/kg·K for 5 T at 17 K), $KTm(MoO_4)_2$[17] (ΔS_θ = 9.8 J/kg·K for 5 T at 10 K), and $KEr(MoO_4)_2$[18] (ΔS_θ = 13 J/kg·K for 5 T at 10 K).

$RCr_{0.5}Fe_{0.5}O_3$ (R = La, …, Lu) compounds crystallize in a disordered orthorhombic-perovskite structure with *Pbnm* space group having randomly distributed Cr^{3+} and Fe^{3+} ions owing to similar ionic radii of Cr^{3+} (0.615 Å) and Fe^{3+} (0.645 Å) ions[19–23]. The canted-antiferromagnetic order emerges in $RFeO_3$ due to the dominant Fe^{3+}-Fe^{3+} exchange couplings ($\Gamma_4(G_xA_yF_z)$ in Bertaut's notation)[24]. In $RCr_{0.5}Fe_{0.5}O_3$, the Γ_4 magnetic structure occurs at much lower T originating from a magnetic dilution effect of Cr^{3+} ions[28]. Extensive investigations on the series of compounds based on diverse magnetic phases and interactions reveal intriguing physical properties, such as metamagnetism[25,26], exchange bias[27,28], magnetodielectric effect[22,29,30], and multiferroicity[31–34]. Additionally,

Department of Physics, Yonsei University, Seoul 03722, Korea. ✉email: eland@yonsei.ac.kr; phylove@yonsei.ac.kr

large cryogenic MCEs in polycrystalline forms, such as $GdCr_{0.5}Fe_{0.5}O_3$[20] (ΔS_M = 29.2 J/kg·K for ΔH = 0–4.5 T), Gd_2NiMnO_6[35] (ΔS_M = 37.2 J/kg·K for ΔH = 0–8 T), $ErCr_{0.5}Fe_{0.5}O_3$[36] (ΔS_M = 12.4 J/kg·K for ΔH = 0–5 T), and $DyCr_{0.5}Fe_{0.5}O_3$[33] (ΔS_M = 11.3 J/kg·K for ΔH = 0–4.5 T) have also been discovered. Various studies have hypothesized that large magnetic moments of magnetic rare-earth ions with strong anisotropy would significantly affect the cryogenic MCE. However, these studies focused only on polycrystalline specimens containing a large number of grains of all spatial orientations resulting in the average effect for observed physical properties.

To investigate the role of magnetic rare-earth ions and influence of anisotropic characteristics on MCE, single crystals of $GdCr_{0.5}Fe_{0.5}O_3$ (GCFO) and $ErCr_{0.5}Fe_{0.5}O_3$ (ECFO) were grown. For GCFO, large Gd^{3+} moments align below T_{Gd} (the ordering temperature of Gd^{3+} moments) = 12 K, which exhibits a relatively isotropic nature. The giant MCE is evidenced by the near-reversible magnetization along and perpendicular to the *c*-axis induces the maximum magnetic entropy change of ΔS_M = 49.8 and 48.8 J/kg·K, respectively. In contrast, Er^{3+} moments aligned along the *c*-axis below T_{Er} (the ordering temperature of Er^{3+} moments) = 11 K give rise to a highly anisotropic MCE. This generates a giant rotational MCE, i.e., ΔS_θ = 20.8 J/kg·K. In view of the distinct magnetic aspects of disordered perovskites, these results contribute to the fundamental and applied research on magnetic materials.

Results and discussion

Figure 1a and 1b show the X-ray diffraction patterns measured at room temperature for the ground GCFO and ECFO, and the simulated patterns analyzed by the Rietveld refinement using the Fullprof software, respectively. The refined results indicate that GCFO and ECFO form an orthorhombic disordered perovskite with the *Pbnm* space group. The lattice constants were observed to be a = 5.3318 Å, b = 5.5674 Å, and c = 7.6379 Å for GCFO and a = 5.2411 Å, b = 5.5451 Å, and c = 7.5496 Å for ECFO. Additional details of crystallographic data are summarized in Table 1. The crystallographic structures of GCFO and ECFO viewed from the *c*- and *a*-axes are depicted in

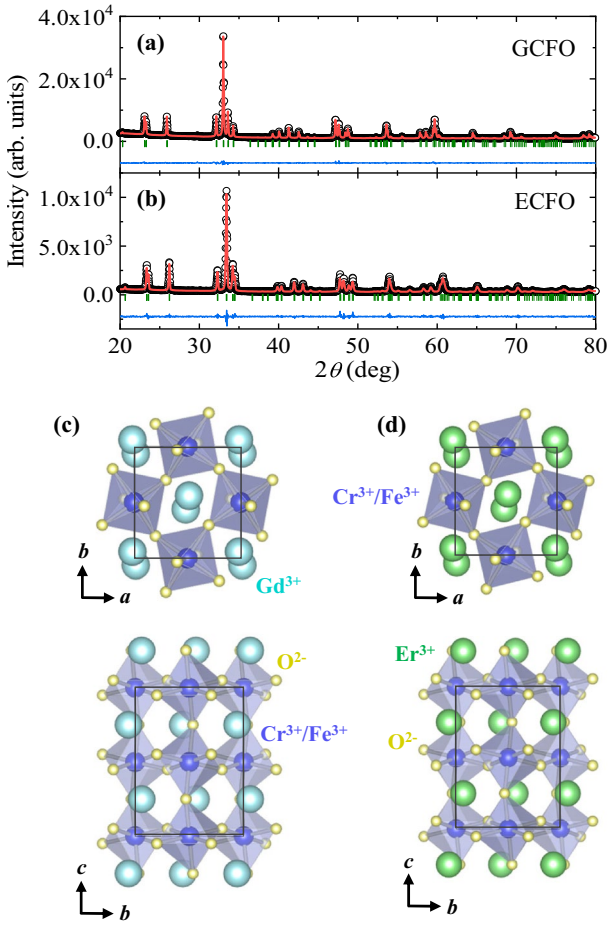

Figure 1. Crystallographic structures of GCFO and ECFO single crystals. (**a**, **b**) Observed (open circles) and calculated (solid line) powder X-ray diffraction patterns for the ground $GdCr_{0.5}Fe_{0.5}O_3$ (GCFO) and $ErCr_{0.5}Fe_{0.5}O_3$ (ECFO) single crystals. The short green lines denote the Bragg positions, and the blue curve indicates the difference between the observed and calculated patterns. (**c**) View of the crystallographic structure of GCFO from the *c*-axis and *a*-axis. The light blue, purple, and yellow spheres represent the Gd^{3+}, Cr^{3+}/Fe^{3+}, and O^{2-} ions, respectively. The black box with the rectangular cross-sections depict a crystallographic unit cell. (**d**) View of the crystallographic structure of ECFO from the *c*-axis and *a*-axis. The green, purple, and yellow spheres represent the Er^{3+}, Cr^{3+}/Fe^{3+}, and O^{2-} ions, respectively.

	$GdCr_{0.5}Fe_{0.5}O_3$	$ErCr_{0.5}Fe_{0.5}O_3$
Structure	Orthorhombic	Orthorhombic
Space group	*Pbnm*	*Pbnm*
a (Å)	5.3318	5.2411
b (Å)	5.5674	5.5451
c (Å)	7.6379	7.5496
V (Å^3)	226.7254	219.4097
Gd /Er(x, y, z)	(0.98452, 0.06061, 0.25)	(0.98180, 0.06865, 0.25)
Cr (x, y, z)	(0.5, 0, 0)	(0.5, 0, 0)
Fe (x, y, z)	(0.5, 0, 0)	(0.5, 0, 0)
O_1 (x, y, z)	(0.09541, 0.46746, 0.25)	(0.10199, 0.46368, 0.25)
O_2 (x, y, z)	(0.70144, 0.29933, 0.05020)	(0.69014, 0.30857, 0.05442)
R_p (%)	9.74	16.1
R_{wp} (%)	7.99	14.7
R_{exp} (%)	6.70	9.52
χ^2	1.42	2.38

Table 1. Crystallographic data of GCFO and ECFO obtained from X-ray diffraction.

Fig. 1c and 1d, respectively. These structures are distinct from a double perovskite in which two different transition metal ions are alternately located in corner-shared octahedral units. Therefore, in disordered perovskites GCFO and ECFO, the sites of Cr^{3+} and Fe^{3+} ions present the randomly distributed arrangement arising from comparable ionic radii. The oxygen octahedral cages are considerably distorted because of the small radius of Gd^{3+}/Er^{3+} ions, resulting in O^{2-} ion shifts in the bonds connecting the Cr^{3+}/Fe^{3+} ions.

To examine the magnetic properties of GCFO and ECFO single crystals, the dependence of T on magnetic susceptibility $\chi = M/H$ was measured at $H = 0.01$ T on warming after zero-field cooling (ZFC) and cooling in the same field (FC). The anisotropic χ's were obtained for the orientations that are parallel ($H//c$) and perpendicular to the c-axis ($H \perp c$), as shown in Fig. 2a and b for GCFO and Fig. 2c and d for ECFO, respectively. Based on a previous study, the canted antiferromagnetic order of Fe^{3+} magnetic moments in $GdFeO_3$ manifests at $T_N = 661$ K[37]. Unlike other orthoferrites, the canted moments along the c-axis do not rotate on further cooling. In GCFO, half of the Fe^{3+} ions are replaced by Cr^{3+} ions. However, the same tendency of canted moments aligned along the c-axis is sustained because χ for $H//c$ appears to be larger than that for $H \perp c$ in the overall T range, except for the low-T regime (Fig. 2a and b). The Gd^{3+} moments in GCFO are antiferromagnetically ordered along magnetic easy-axis c in the low-T region, evidenced by the smaller magnitude and peaky feature of χ for $H//c$. Even without an orbital moment ($L = 0$ of Gd), Gd compounds still possess a very small magnetic anisotropy due to weak dipole–dipole interaction of the large Gd spin. This weak anisotropy is the reason why the Gd spins are pointing towards the c-axis, i.e., a particular easy-axis[38].

In $ErFeO_3$, the canted antiferromagnetic order of Fe^{3+} magnetic moments with a small net moment aligned along the c-axis occurs at $T_N \approx 640$ K[39,40] with Γ_4 magnetic structure[41]. On further cooling, the net magnetic moment rotates to the a-axis by 90° at $T_{SR} = 113$ K by forming the $\Gamma_2(F_xC_yG_z)$ magnetic structure, followed by the long range antiferromagnetic order of Er^{3+} magnetic moments aligned along the c-axis ($\Gamma_1(C_z$-type order)) at $T = 3.4$ K[42,43]. In ECFO, the χ properties of $H//c$ and $H \perp c$ directions in the overall T range are strikingly different because of the strong anisotropic nature of the system (Fig. 2c and d). In contrast to the GCFO, the ECFO exhibits spin reorientation transition at $T_{SR,1} \approx 180$ K, which indicates a considerable decrease in χ along the c-axis and an escalation of χ perpendicular to the c-axis. As shown in Fig. 3, we constructed the Belov-Arrott plot to determine the order of magnetic phase transition at $T_{SR,1} \approx 180$ K. The slope was found to be positive for the overall regime of spin-reorientation, which suggests a second-order phase transition[44,45]. However, EFCO also exhibits signatures of a first-order phase transition such as thermally hysteretic behavior between ZFC and FC data (Fig. 2c) and the absence of a distinct peak in the specific heat (Fig. 2f). Thus, further studies are required to clearly identify the order of this spin-reorientation transition[46,47]. As T was further decreased, sharp anomalies were observed around 10 K indicating the antiferromagnetic order of Er^{3+} moments.

The T dependence of the heat capacity divided by T (C/T) measured at $H = 0$ T for GCFO exhibits a sharp increase below $T_{Gd} = 12$ K, indicating the ordering of Gd^{3+} moments, as shown in Fig. 2e. The influence of the ordering of magnetic Gd^{3+} moments on C/T in the low T regime was estimated by subtracting the contributions from Cr^{3+} and Fe^{3+} ions below T_{Gd}. The subtracted part of C/T was obtained from the following equation:

$$C/T \sim \gamma + \rho T^{1/2} + \beta T^2, \tag{1}$$

where γ, ρ, andβ are coefficients corresponding to the electron, magnon, and phonon contributions of the Cr^{3+} and Fe^{3+} moments, respectively. Fitting the data to Eq. (1) resulted in the grey curve of C/T in the inset of Fig. 2e, which indicates the contribution from the interactions of Fe^{3+}–Fe^{3+}, Cr^{3+}–Cr^{3+} and Cr^{3+}–Fe^{3+} pairs and the interaction between the Gd^{3+} and Cr^{3+}/Fe^{3+} sublattices at low T. The estimated entropy change based solely on the order of Gd^{3+} moments ΔS_{Gd} in zero H was observed to be 7.5 J/mole·K. ΔS_{Gd} is 21.7% of the expected

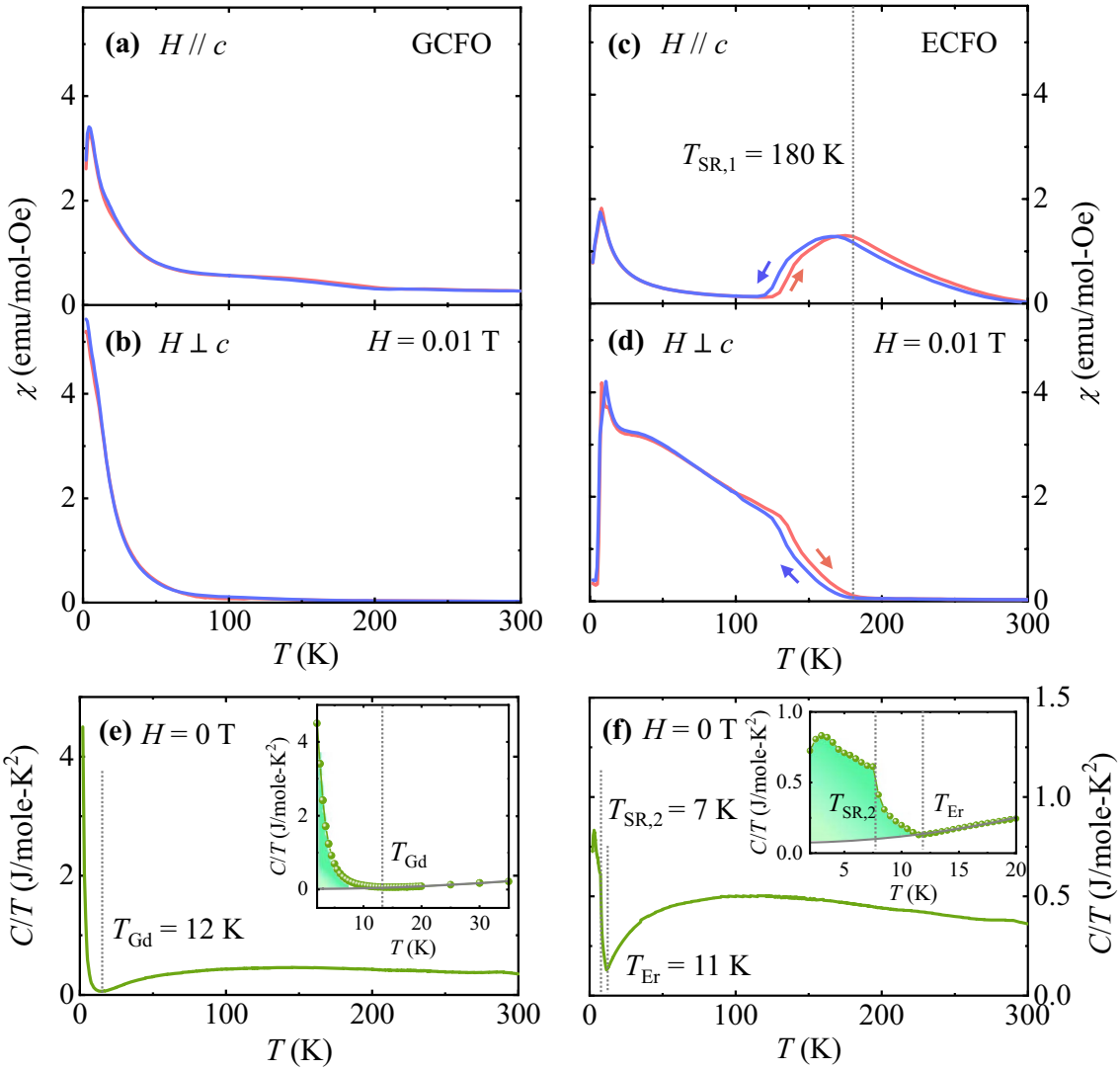

Figure 2. Magnetic susceptibility and heat capacity. (**a**, **b**) Temperature (T) dependence of magnetic susceptibility $\chi = M/H$ of single crystalline GCFO at $H = 0.01$ T measured on heating from 2 to 300 K after zero-field cooling (ZFC) and upon cooling at the same field (FC) parallel ($H//c$) and perpendicular ($H \perp c$) to the c-axis. (**c**, **d**) T dependence of magnetic susceptibility $\chi = M/H$ of single crystalline ECFO at $H = 0.01$ T measured on heating from 2 to 300 K after ZFC and FC for $H//c$ and $H \perp c$. (**e**) Heat capacity divided by temperature (C/T) measured at $H = 0$ T and $T = 2$–300 K for GCFO. Inset shows C/T in the $T = 2$–35 K region. The gray curve was obtained by fitting, considering the influence of Cr^{3+}/Fe^{3+} moments on C/T at a low-T regime. The vertical dashed line denotes the ordering T of Gd^{3+} moments as $T_{Gd} = 12$ K. The colored area indicates the contribution of Gd^{3+} ions to the magnetic entropy. (**f**) C/T measured at $H = 0$ T and $T = 2$–300 K for ECFO. Inset shows C/T in the $T = 2$–20 K region. The gray curve was obtained by fitting, considering the influence of Cr^{3+}/Fe^{3+} moments on C/T at a low-T regime. The vertical dashed lines designate the ordering T of Er^{3+} moments as $T_{Er} = 11$ K and the 2nd spin-reorientation transition of Cr^{3+}/Fe^{3+} moments, $T_{SR,2} = 7$ K. The colored area indicates the contribution of Er^{3+} ions to the magnetic entropy.

value of fully-saturated Gd^{3+} moments, i.e., $2R\ln(2J + 1) = 34.6$ J/mole·K, where R is the gas constant and J is the total angular momentum ($J = 7/2$ for Gd^{3+} ions).

Previous experimental studies on neutron diffraction on the polycrystalline ECFO suggest that the spin configuration transforms from representation $\Gamma_4(G_xA_yF_z)$ to $\Gamma_2(F_xC_yG_z)$ on lowering T across $T_{SR,1}$[26]. During the ordering of Er^{3+} moments at $T_{Er} = 11$ K, the C_z component belonging to Γ_1 was observed on the Er^{3+} sublattice. Further decrease in T causes the 2nd spin-reorientation transition at $T_{SR,2} = 7$ K on the Cr^{3+}/Fe^{3+} sublattice where the G_y component identified as another Γ_1 phase. Across $T_{SR,2}$, larger Er^{3+} moments were also observed. Furthermore, the measured C/T value reveals two different transitions, i.e., T_{Er} and $T_{SR,2}$ at low-T regime, as shown in the inset of Fig. 2f. After subtracting the contribution of the Cr^{3+}/Fe^{3+} sublattice represented by the gray curve, ΔS_{Er} in zero H was estimated to be 4.11 J/mole·K, which is 8.9% of the expected value of the fully saturated Er^{3+} moments, $2R\ln(2J + 1) = 46.1$ J/mole·K ($J = 15/2$ for the Er^{3+} ions).

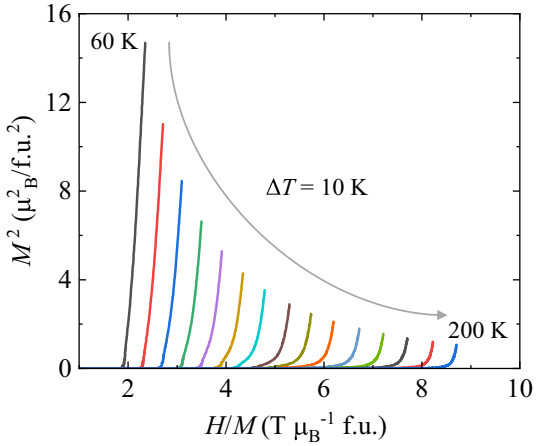

Figure 3. Belov-Arrott plot. Belov-Arrot plot for the ECFO crystal at *H*//*c* and *T* = 60—200 K.

As shown in Fig. 4, the magnetic anisotropies in GCFO and ECFO were investigated using isothermal *M* for two different orientations (*H*//c and $H \perp c$) at 2 K, the former exhibiting an insignificant magnetic anisotropy. The initial *M* curve at *H*//*c* shows a weak magnetic transition at *H* = 0.85 T (Fig. 4a), suggesting a spin-flop transition because of the G_z component that is consistent with the transition observed in a previous study of the polycrystalline ECFO[26]. The value of *M* at a maximum *H* of 9 T is 6.75 $_{\mu B}$/f.u. The consecutive sweeping of *H* reveals no hysteretic behavior with nearly zero remanent *M* and coercive field. The initial *M* curve at $H \perp c$ increases smoothly (Fig. 4b) and attains the same magnitude of *M* at 9 T as that at *H*//*c*. Contrarily, ECFO has a distinctive *H* dependence for each direction. The slope of the isothermal *M* curve for *H*//*c* is the greatest in the narrow *H* regime between 0.3 and 1.0 T; thereafter, it decreases and the *M* value is observed to be 7.32 μ_B/f.u. at 9 T. However, the initial *M* curve for $H \perp c$ varies smoothly and does not reach saturation at *H* up to 9 T. The *M* value at 9 T is found to be 3.58 μ_B/f.u., which is approximately half the value of *M* at 9 T for *H*//*c*.

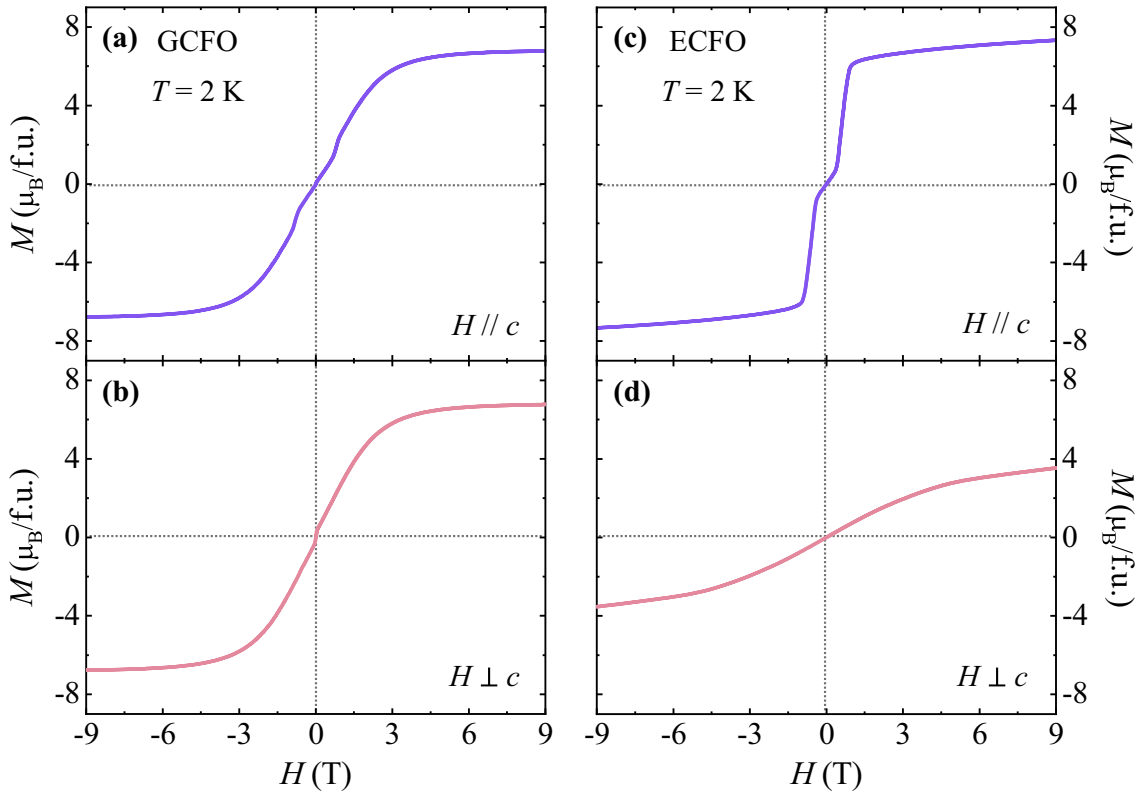

Figure 4. Isothermal magnetization. (**a**, **b**) Full magnetic hysteresis curve of the isothermal magnetization measured at 2 K up to $H = \pm 9$ T at *H*//*c* and $H \perp c$, respectively, for GCFO. (**c**, **d**) Full magnetic hysteresis curve of the isothermal magnetization measured at 2 K up to $H = \pm 9$ T at *H*//*c* and $H \perp c$, respectively, for GCFO.

In GCFO, same M values at the maximum H and similar shapes of M curves for different orientations imply the moderately isotropic nature of the Gd^{3+} moments associated with the half-filled 4f. electronic configuration ($S = 7/2$ and $L = 0$). Therefore, the crystal field effect affected by the symmetry of local environment can be minimum[48–50]. Contrarily, the Er^{3+} ion exhibits strong anisotropic properties in the ECFO system because its angular momentum ($L = 6$) breaks the local symmetry and the crystal field effect substantially affects the magnetocrystalline anisotropy[43,50].

The contrasting magnetic properties of GCFO and ECFO lead to different MCE characteristics measured using the initial M curves with dense T steps for $T = 2$–30 K, as shown in Fig. 5. In GCFO, the almost isotropic magnetic properties resulted in the typical decreasing trend of the M values similarly for the two different orientations as T is increased (Fig. 5a and 5b). For $H//c$ in ECFO, rapid increase in the initial M curve in the low-H regime at 2 K becomes broaden as T increases; hence, the M value at low H is lower than that at higher T, as plotted in the inset of Fig. 5c. This characteristic of the initial M curves varies above 10 K; thus, the M value exhibits a typical reduction in most of the H regime as T increases. At $H \perp c$, owing to the smaller magnitude and smooth variation of M values, the overall magnitude of M is reduced marginally but continually in the entire regime of H as T increases (Fig. 5d).

The MCE in GCFO and ECFO was quantified by calculating the isothermal magnetic entropy change, ΔS_M, at a given T using the Maxwell's relation:

$$\Delta S_M(T,H) = -\mu_0 \int_0^{H_f} \frac{\partial M(T,H)}{\partial T} dH, \tag{2}$$

where μ_o is the magnetic permeability of free space, H_f is the end point of H for the integral ($H_f = 3$, 5, 7, and 9 T), and the T gradient of M. $\frac{\partial M(T,H)}{\partial T}$ was estimated using the slope of two consecutive data points. The T-dependence of estimated $\Delta S_M(T)$ for $H//c$ and $H \perp c$ is plotted in Fig. 6, for the H regimes of $\Delta H = 0$–3, 0–5, 0–7, and 0–9 T respectively. The ΔS_M values for both orientations in GCFO present the largest at 4 K, where the maximum ΔS_M for $\Delta H = 0$–9 T were achieved as 49.8 and 48.8 J/kg·K, respectively, for $H//c$ and $H \perp c$ (Fig. 6a and b). This value of ΔS_M is greater than that of the other oxide materials, such as Dy_2CoMnO_6[51] ($\Delta S_M = 9.3$ J/kg·K for $\Delta H = 0$–7 T), $HoMnO_3$[52] ($\Delta S_M = 13.1$ J/kg·K for $\Delta H = 0$–7 T), $GdCrO_4$[53] ($\Delta S_M = 29.0$ J/kg·K for $\Delta H = 0$–9 T), and $HoCrO_4$[54] ($\Delta S_M = 31.0$ J/kg·K for $\Delta H = 0$–8 T). Furthermore, non-hysteretic behavior of isothermal M indicates the absence of unnecessary ΔS_M loss.

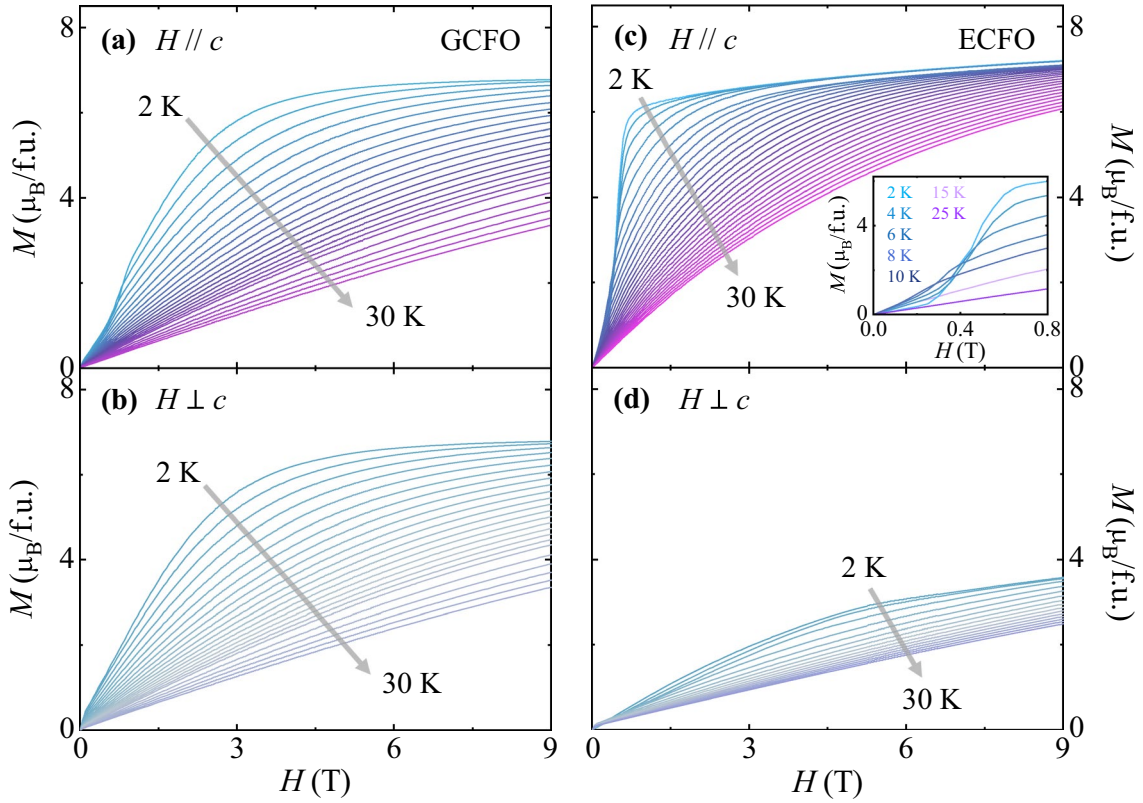

Figure 5. Initial curves of isothermal magnetization. (**a**, **b**) Initial curves of the isothermal magnetization for $H//c$ and $H \perp c$, respectively, at temperatures varying from 2 to 30 K for GCFO. (**c**, **d**) Initial curves of the isothermal magnetization for $H//c$ and $H \perp c$, respectively, at temperatures varying from 2 to 30 K for ECFO. Inset of c shows the initial curves of magnetization in the low-H region for $T = 2$, 4, 6, 8, 10, 15, and 25 K.

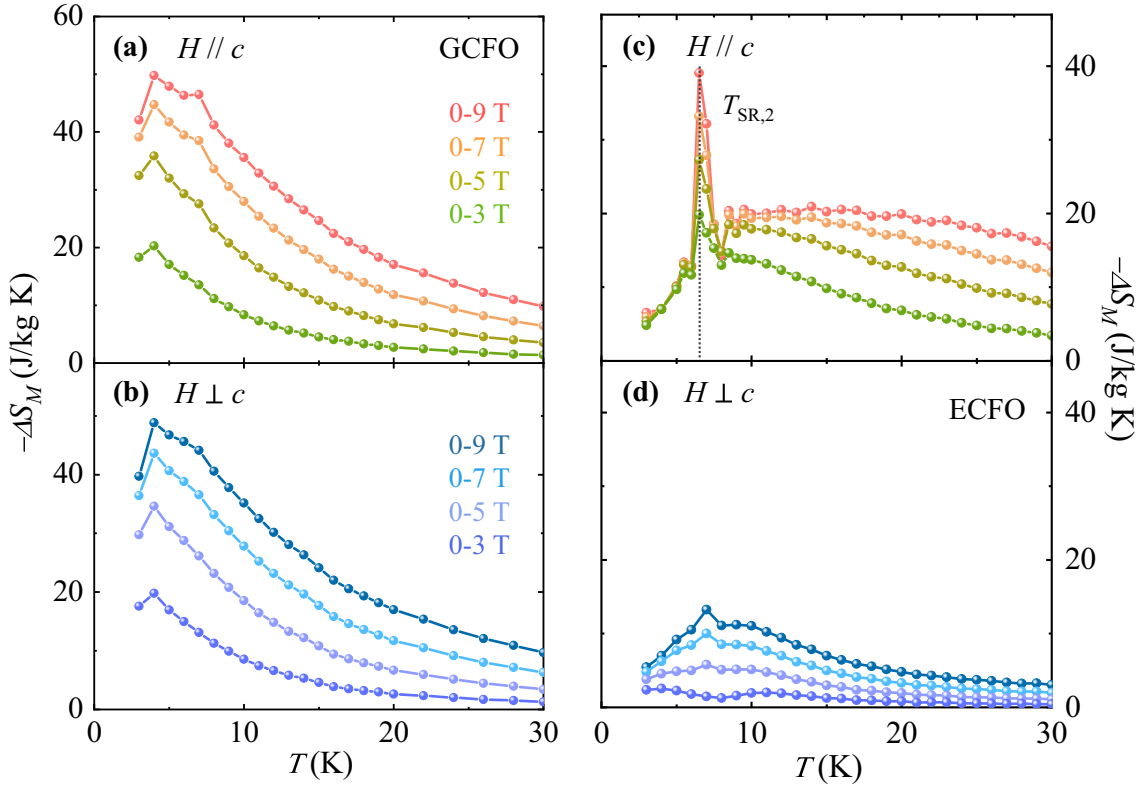

Figure 6. Anisotropic magnetocaloric effect in GCFO and ECFO crystals. (**a**, **b**) Anisotropic magnetocaloric effect in GCFO. T dependence of magnetic entropy change $-\Delta S_M$ for $H//c$ and $H \perp c$ with H regimes of ΔH = 0–3, 0–5, 0–7, and 0–9 T, obtained by integrating the T gradient of the initial magnetization curves in Fig. 4a and b, respectively. (**c**, **d**) Anisotropic magnetocaloric effect in ECFO. T dependence of magnetic entropy change $-\Delta S_M$ for $H//c$ and $H \perp c$ with H regimes of ΔH = 0–3, 0–5, 0–7, and 0–9 T, obtained by integrating the T gradient of the initial magnetization curves in Fig. 4c and d, respectively.

In ECFO, the peculiar anisotropy of ΔS_M was observed because the Er^{3+} spins mainly aligned along the c-axis. The intercrossed isothermal M values in the low-H regime for $H//c$ (inset of Fig. 5c) considerably cancelled ΔS_M; hence, ΔS_M for ΔH = 0–9 T was calculated to be 6.5 J/kg·K at 3 K (Fig. 6c). As T increases further, ΔS_M continues to increase and peaks sharply at $T_{SR,2}$ with a maximum ΔS_M value of 39.1 J/kg·K. This feature was derived from the largest drop of isothermal M across $T_{SR,2}$, which was verified by measuring initial M curves repeatedly in the low-T regime for various samples of ECFO crystals. Above $T_{SR,2}$, ΔS_M shows a broad variation and its value is approximately 20 J/kg·K. In contrast with ΔS_M for $H//c$, the overall magnitude of ΔS_M for $H \perp c$ is largely reduced and its maximum value turns out to be 13.2 J/kg·K for ΔH = 0–9 T (Fig. 6d). Additionally, ΔS_M was estimated up to T = 200 K for investigating the influence of χ variation at H = 0.01 T across the spin-reorientation transition of $T_{SR,1}$ (Figs. 2c and d). As shown in Fig. 7, magnitude and anisotropy of the estimated ΔS_M relevant to the spin-reorientation of Cr^{3+}/Fe^{3+} moments were not pronounced. We also estimated relative cooling power (RCP) for both GCFO and ECFO crystals to show the potential of our single crystals as magnetic cryo-refrigerant. The RCP can be expressed by the following equation,

$$\mathrm{RCP} = \int_{T_{\mathrm{cold}}}^{T_{\mathrm{hot}}} \Delta S_M(T) dT, \tag{3}$$

where T_{cold} = 2 K and T_{hot} was determined by the full width half maximum in ΔS_M. Due to the rather isotropic nature of MCE, the RCP in the GCFO was estimated as 301 and 309 J/ kg at $H//c$ and $H \perp c$, respectively, for ΔH = 0–9 T. On the other hand, the RCP in the ECFO was found to be 623 J/kg at $H//c$ and 169 J/kg at $H \perp c$. The RCP has been estimated in polycrystalline specimens such as $La_{0.67}Sr_{0.22}Ba_{0.11}Mn_{0.9}Fe_{0.1}O_3$[55] (241 J/kg for ΔH = 0–5 T), $La_{0.57}Mg_{0.23}MnO_3$[56] (176 J/kg for ΔH = 0–5 T), $Ni_{0.5}Zn_{0.5}Fe_2O_4$[57] (161 J/kg for ΔH = 0–2.5 T) and $La_{0.5}Pr_{0.2}Ca_{0.1}Sr_{0.2}MnO_3$[58] (372 J/kg for ΔH = 0–5 T), and in single crystals such as $La_{0.7}Ca_{0.3}MnO_3$[59] (358 J/kg for ΔH = 0–5 T), h-$DyMnO_3$[60] (300 J/kg for ΔH = 0–5 T) and $GdScO_3$[61] (307 J/kg) for ΔH = 0–7 T).

To employ the conspicuous characteristics of the anisotropic MCE in disordered-perovskite ECFO, the rotating MCE was detected using the angle dependence of ΔS_M, which is denoted by ΔS_θ, where θ is the angle deviated from the c-axis (θ = 0° for $H//c$, and θ = 90° for $H \perp c$), as shown in the inset of Fig. 7. Figure 8 displays the resulting ΔS_θ taken at T = 3, 7, 10 and 29 K for H = 9 T. The dissimilar T dependence of ΔS_M between $H//c$ and $H \perp c$ in the low T regime (Fig. 6c and d) engenders the angle-dependent modulation of ΔS_θ, which changes significantly with T. ΔS_θ at 3 K alters negligibly with θ rotation; however, ΔS_θ at $T_{SR,2}$ = 7 K shows a sudden increase to 15°. The

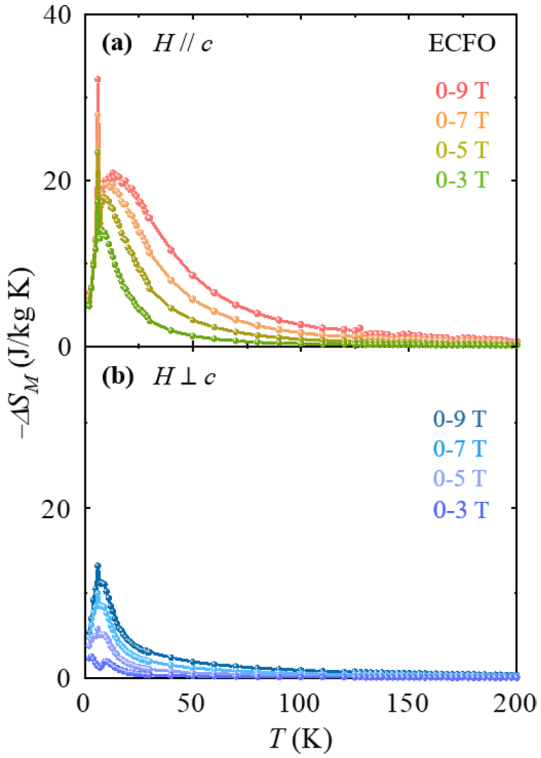

Figure 7. Anisotropic magnetic entropy change in ECFO. (**a**) T dependence of magnetic entropy change $-\Delta S_M$ for $H//c$ with magnetic field regimes of $\Delta H = 0$–3, 0–5, 0–7, and 0–9 T, respectively, obtained by integrating the T gradient of the initial magnetization curves in ECFO in the range $T = 2$–200 K. (**b**) T dependence of magnetic entropy change $-\Delta S_M$ for $H \perp c$ with magnetic field regimes of $\Delta H = 0$–3, 0–5, 0–7, and 0–9 T, respectively, obtained by integrating the T gradient of the initial magnetization curves in ECFO in the range $T = 2$–200 K.

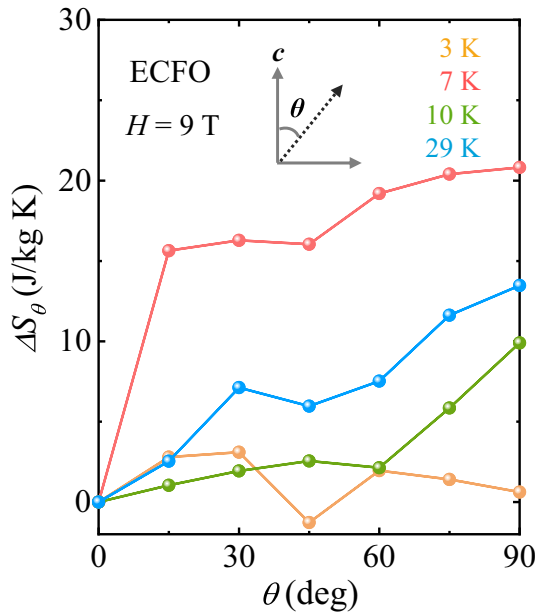

Figure 8. Rotating magnetocaloric effect in ECFO. Angular dependence of magnetic entropy change ΔS_θ at $T = 3$, 7, 10, and 29 K with $\Delta H = 0$–9 T, respectively. θ is the angle deviating from the c-axis, i.e., $\theta = 0°$ for $H//c$ and 90° for $H \perp c$.

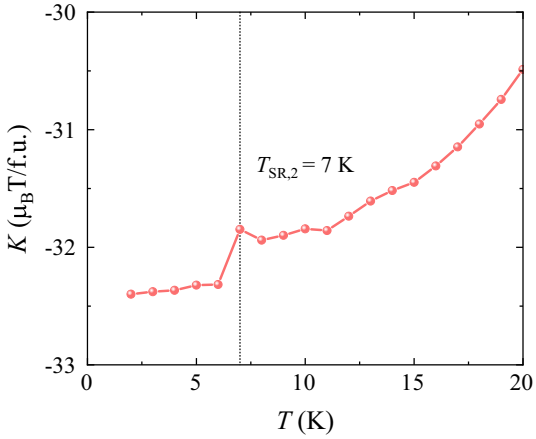

Figure 9. Magnetic anisotropy constant. Temperature dependence of magnetic anisotropy constant K.

continued variation in ΔS_θ with θ yields a large rotational MCE demonstrated by the maximum change of ΔS_θ = 20.8 J/kg·K, which would have applications in the rotary magnetic refrigerator technology. We have estimated the magnetic anisotropy constant for the ECFO crystal. The magnetic free energy of the ECFO crystal with uniaxial magnetocrystalline anisotropy can be described by $F = K\sin^2\theta - MH\cos\theta$, where the first term indicates the magnetic anisotropy energy with the angle θ deviating from the c axis and the second term denotes the Zeeman energy. The magnetic anisotropy constant K was determined by the Sucksmith and Thompson method[62], based on the experimental data for the ECFO crystal. The result shown in Fig. 9 exhibits a clear feature at $T_{SR,2}$ = 7 K[63]. As T increases further, the gradual increase of ΔS_θ with θ demonstrates a maximum ΔS_θ of 9.9 and 13.5 J/kg·K at 10 and 29 K, respectively.

Conclusion

This study investigated the anisotropic magnetic and magnetocaloric properties of disordered-perovskite $GdCr_{0.5}Fe_{0.5}O_3$ and $ErCr_{0.5}Fe_{0.5}O_3$. In $GdCr_{0.5}Fe_{0.5}O_3$, the limited isotropic nature of Gd^{3+} moments owing to zero orbital angular momentum creates a weak directional dependence of giant magnetocaloric effect, characterized by maximum magnetic entropy changes of ΔS_M = 49.8 and 48.8 J/kg·K along and perpendicular to the c-axis, respectively. Non-magnetic hysteretic behavior of isothermal magnetization indicates the absence of dispensable loss of magnetocaloric effect. In contrast, $ErCr_{0.5}Fe_{0.5}O_3$ reveals the sharpened feature of ΔS_M that is derived from the largest reduction of isothermal magnetization between adjacent measuring temperatures across the 2nd spin-reorientation along the c-axis at $T_{SR,2}$ = 7 K. This particular anisotropy causes large rotary magnetocaloric effect with a maximum entropy change of ΔS_θ = 20.8 J/kg·K. The results on different anisotropic magnetic properties of the disordered-perovskite compounds provide insights into suitable materials for magnetic functional applications.

Methods

Single crystals of GCFO and ECFO were synthesized using conventional flux method with PbO, PbO_2, and PbF_2 fluxes in a high-T furnace. The stoichiometric ratios of Gd_2O_3/Er_2O_3, Cr_2O_3, and Fe_2O_3 powders for GCFO and ECFO were mixed and ground using a pestle in a corundum mortar. The mixture was pelletized and calcined at 1000 °C for 12 h. The calcined pellet was finely re-ground, pelletized, and sintered at 1200 °C for 12 h. The same procedure was repeated at 1250 °C for 24 h. The pre-sintered power containing fluxes was heated to 1260 °C in a platinum crucible for 24 h until it was completely dissolved. Thereafter, it was slowly cooled to 850 °C at the rate of 2 °C/h and further cooled to room temperature T at the rate of 100 °C/h. To identify the crystallographic structures of GCFO and ECFO crystals, X-ray diffraction was performed using an X-ray diffractometer (Ultima IV, Rigaku Corp., Japan) with Cu-K_α radiation.

The T and H dependences of DC magnetization (M) were obtained using a vibrating sample magnetometer at T = 2–300 K and H = -9–9 T in a physical properties measurement system (PPMS, Quantum Design, Inc., USA). The dependence of T on specific heat (C) was measured using the standard relaxation method and PPMS.

Data availability

The data that support the findings of this study are available from the corresponding authors upon reasonable request. The datasets associated with the crystallographic structures that are analyzed in this study are available in the Crystallography Open Database (COD) repository, #3,000,434 (https://www.crystallography.net/cod/information_card.php?id=3000434&CODSESSION=cbg4dlc90k4ciiuucsm3fkq2a3) and #3,000,435 (https://www.crystallography.net/cod/information_card.php?id=3000435&CODSESSION=cbg4dlc90k4ciiuucsm3fkq2a3).

Received: 12 November 2022; Accepted: 26 April 2023
Published online: 02 May 2023

References

1. Pecharsky, V. K. & Gschneidner, K. A. Jr. Magnetocaloric effect and magnetic refrigeration. *J. Magn. Magn. Mater.* **200**, 44–56. https://doi.org/10.1016/S0304-8853(99)00397-2 (1999).
2. de Oliveira, N. A. & von Ranke, P. J. Theoretical aspects of the magnetocaloric effect. *Phys. Rep.* **489**, 89–159. https://doi.org/10.1016/j.physrep.2009.12.006 (2010).
3. Franco, V. *et al.* Magnetocaloric effect: From materials research to refrigeration devices. *Prog. Mater. Sci.* **93**, 112–232. https://doi.org/10.1016/j.pmatsci.2017.10.005 (2018).
4. Evangelisti, M. *et al.* Cryogenic magnetocaloric effect in a ferromagnetic molecular dimer. *Angew. Chem. Int. Ed. Engl.* **50**, 6606–6609. https://doi.org/10.1002/anie.201102640 (2011).
5. Phan, M.-H. & Yu, S.-C. Review of the magnetocaloric effect in manganite materials. *J. Magn. Magn. Mater.* **308**, 325–340. https://doi.org/10.1016/j.jmmm.2006.07.025 (2007).
6. Ram, N. R. *et al.* Review on magnetocaloric effect and materials. *J. Supercond. Nov. Magn.* **31**, 1971–1979. https://doi.org/10.1007/s10948-018-4666-z (2018).
7. Zhang, Y. *et al.* Magnetic properties and giant cryogenic magnetocaloric effect in B-site ordered antiferromagnetic Gd_2MgTiO_6 double perovskite oxide. *Acta. Mater.* **226**, 117669. https://doi.org/10.1016/j.actamat.2022.117669 (2022).
8. Moon, J. Y., Kim, M. K., Choi, Y. J. & Lee, N. Giant anisotropic magnetocaloric effect in double-perovskite Gd_2CoMnO_6 single crystals. *Sci. Rep.* **7**, 16099. https://doi.org/10.1038/s41598-017-16416-z (2017).
9. Yin, C. *et al.* Unusual oxidation states give reversible room temperature magnetocaloric effect on perovskite-related oxides $SrFe_{0.5}Co_{0.5}O_3$. *J. Solid State Chem.* **184**, 3228–3231. https://doi.org/10.1016/j.jssc.2011.10.002 (2011).
10. Balli, M. *et al.* Magnetocaloric properties of the hexagonal $HoMnO_3$ single crystal revisited. *Physica B Condens.* **478**, 77–83. https://doi.org/10.1016/j.physb.2015.08.063 (2015).
11. Zhang, X., Chen, Y., Lü, L. & Li, Z. A potential oxide for magnetic refrigeration application: CrO_2 particles. *J. Phys.: Condens. Matter* **18**, L559. https://doi.org/10.1088/0953-8984/18/44/L01 (2006).
12. Moon, J. Y. *et al.* Anisotropic magnetic properties and giant rotating magnetocaloric effect in double-perovskite Tb_2CoMnO_6. *Phys. Rev. B* https://doi.org/10.1103/PhysRevB.98.174424 (2018).
13. Nikitin, S. A., Skokov, K. P., Koshkidko, Y. S., Pastushenkov, Y. G. & Ivanova, T. I. Giant rotating magnetocaloric effect in the region of spin-reorientation transition in the $NdCo_5$ single crystal. *Phys. Rev. Lett.* **105**, 137205. https://doi.org/10.1103/PhysRevLett.105.137205 (2010).
14. Jin, J.-L. *et al.* Giant anisotropy of magnetocaloric effect in $TbMnO_3$ single crystals. *Phys. Rev. B* **83**, 184431. https://doi.org/10.1103/PhysRevB.83.184431 (2011).
15. Balli, M., Jandl, S., Fournier, P. & Gospodinov, M. M. Anisotropy-enhanced giant reversible rotating magnetocaloric effect in $HoMn_2O_5$ single crystals. *Appl. Phys. Lett.* **104**, 232402. https://doi.org/10.1063/1.4880818 (2014).
16. Ke, Y.-J., Zhang, X.-Q., Ma, Y. & Cheng, Z.-H. Anisotropic magnetic entropy change in $RFeO_3$ single crystals(R = Tb, Tm, or Y). *Sci. Rep.* **6**, 19775. https://doi.org/10.1038/srep19775 (2016).
17. Tarasenko, R., Tkáč, V., Orendáčová, A., Orendáč, M. & Feher, A. Experimental study of the rotational magnetocaloric effect in $KTm(MoO_4)_2$. *Phys. B Condens.* **538**, 116–119. https://doi.org/10.1016/j.physb.2018.03.027 (2018).
18. Tkáč, V. *et al.* Giant reversible rotating cryomagnetocaloric effect in $KEr(MoO_4)_2$ induced by a crystal-field anisotropy. *Phys. Rev. B* **92**, 024406. https://doi.org/10.1103/PhysRevB.92.024406 (2015).
19. Pomiro, F. *et al.* Spin reorientation, magnetization reversal, and negative thermal expansion observed in $RFe_{0.5}Cr_{0.5}O_3$ perovskites (R=Lu, Yb, Tm). *Phys. Rev. B* **94**, 134402. https://doi.org/10.1103/PhysRevB.94.134402 (2016).
20. Yin, L. H. *et al.* Magnetocaloric effect and influence of Fe/Cr disorder on the magnetization reversal and dielectric relaxation in $RFe_{0.5}Cr_{0.5}O_3$ systems. *Appl. Phys. Lett.* **110**, 192904. https://doi.org/10.1063/1.4983363 (2017).
21. Yin, L. H. *et al.* Multiple temperature-induced magnetization reversals in $SmCr_{1-x}Fe_xO_3$ system. *Mater. Res. Bull.* **48**, 4016–4021. https://doi.org/10.1016/j.materresbull.2013.06.016 (2013).
22. Shin, H. J., Lee, N. & Choi, Y. J. Nonlinear magnetodielectric effect of disordered perovskite $HoCr_{0.5}Fe_{0.5}O_3$: Role of magnetic rare-earth ions. *J. Alloys Compd.* **785**, 1166–1172. https://doi.org/10.1016/j.jallcom.2019.01.291 (2019).
23. Mao, J. *et al.* Temperature- and magnetic-field-induced magnetization reversal in perovskite $YFe_{0.5}Cr_{0.5}O_3$. *Appl. Phys. Lett.* **98**, 192510. https://doi.org/10.1063/1.3590714 (2011).
24. Bertaut, E. F. in *Spin Arrangements and Crystal Structure, Domains, and Micromagnetics* (eds George T. Rado & Harry Suhl) 149–209 (Academic Press, 1963).
25. Nair, V. G., Pal, L., Subramanian, V. & Santhosh, P. N. Structural, magnetic, and magnetodielectric studies of metamagnetic $DyFe_{0.5}Cr_{0.5}O_3$. *J. Appl. Phys.* **115**, 17D728. https://doi.org/10.1063/1.4870139 (2014).
26. Bolletta, J. P. *et al.* Spin reorientation and metamagnetic transitions in $RFe_{0.5}Cr_{0.5}O_3$ perovskites (R=Tb, Dy, Ho, Er). *Phys. Rev. B* **98**, 134417. https://doi.org/10.1103/PhysRevB.98.134417 (2018).
27. Sharannia, M. P. *et al.* Observation of magnetization and exchange bias reversals in $NdFe_{0.5}Cr_{0.5}O_3$. *J. Magn. Magn. Mater.* **430**, 109–113. https://doi.org/10.1016/j.jmmm.2016.12.035 (2017).
28. Hou, L., Shi, L., Zhao, J., Tong, R. & Xin, Y. Insight into the magnetization reversal and exchange bias in $RFe_{0.5}Cr_{0.5}O_3$ ceramics. *J. Phys. Chem. C* **125**, 7950–7958. https://doi.org/10.1021/acs.jpcc.1c00562 (2021).
29. Mandal, P. *et al.* Spin-reorientation, ferroelectricity, and magnetodielectric effect in YFe1-xMnxO_3 ($0.1 \le x \le 0.40$). *Phys. Rev. Lett.* **107**, 137202. https://doi.org/10.1103/PhysRevLett.107.137202 (2011).
30. Kumar, A. *et al.* Origin of natural and magnetic field induced polar order in orthorhombic $PrFe_{1/2}Cr_{1/2}O_3$. *Phys. Rev. B* **104**, 035101. https://doi.org/10.1103/PhysRevB.104.035101 (2021).
31. Tokunaga, Y. *et al.* Composite domain walls in a multiferroic perovskite ferrite. *Nat. Mater.* **8**, 558–562. https://doi.org/10.1038/nmat2469 (2009).
32. Das, N. *et al.* Pr_2FeCrO_6: A type I multiferroic. *Inorg. Chem.* **56**, 12712–12718. https://doi.org/10.1021/acs.inorgchem.7b01086 (2017).
33. Yin, L. H. *et al.* Multiferroicity and magnetoelectric coupling enhanced large magnetocaloric effect in $DyFe_{0.5}Cr_{0.5}O_3$. *Appl. Phys. Lett.* https://doi.org/10.1063/1.4862665 (2014).
34. Lohr, J. *et al.* Multiferroic properties of $RFe_{0.5}Cr_{0.5}O_3$ with R=Tm, Er, Ho, Dy, and Tb. *Phys. Rev. B* **98**, 134405. https://doi.org/10.1103/PhysRevB.98.134405 (2018).
35. Ali, A., Pasrija, K., Sharma, G., Kumar, S. & Singh, Y. Rare-earth tuned magnetism and magnetocaloric effects in double perovskites R_2NiMnO_6. *J. Phys.: Condens. Matter* **34**, 095803. https://doi.org/10.1088/1361-648X/ac3e9e (2022).
36. Yadav, K., Kaur, G., Sharma, M. K. & Mukherjee, K. Magnetocaloric effect and spin-phonon correlations in $RFe_{0.5}Cr_{0.5}O_3$ (R = Er and Yb) compounds. *Phys. Lett. A* **384**, 126638. https://doi.org/10.1016/j.physleta.2020.126638 (2020).
37. Treves, D. Studies on orthoferrites at the Weizmann institute of science. *J. Appl. Phys.* **36**, 1033–1039. https://doi.org/10.1063/1.1714088 (1965).
38. Rotter, M. *et al.* Dipole interaction and magnetic anisotropy in gadolinium compounds. *Phys. Rev. B* **68**, 144418. https://doi.org/10.1103/PhysRevB.68.144418 (2003).
39. Eibschütz, M., Shtrikman, S. & Treves, D. Mössbauer studies of Fe^{57} in orthoferrites. *Phys. Rev.* **156**, 562–577. https://doi.org/10.1103/PhysRev.156.562 (1967).

40. Zhou, Z., Guo, L., Yang, H., Liu, Q. & Ye, F. Hydrothermal synthesis and magnetic properties of multiferroic rare-earth orthoferrites. *J. Alloys Compd.* **583**, 21–31. https://doi.org/10.1016/j.jallcom.2013.08.129 (2014).
41. Gorodetsky, G. *et al.* Magnetic structure of ErFeO3 below 4.5K. *Phys. Rev. B* **8**, 3398–3404. https://doi.org/10.1103/PhysRevB.8.3398 (1973).
42. Sasani, A., Iñiguez, J. & Bousquet, E. Magnetic phase diagram of rare-earth orthorhombic perovskite oxides. *Phys. Rev. B* **104**, 064431. https://doi.org/10.1103/PhysRevB.104.064431 (2021).
43. White, R. L. Review of recent work on the magnetic and spectroscopic properties of the rare-earth orthoferrites. *J. Appl. Phys.* **40**, 1061–1069. https://doi.org/10.1063/1.1657530 (1969).
44. Gamża, M. B. *et al.* Complex magnetic phase diagram of metamagnetic MnPtSi. *Phys. Rev. B* **100**, 014423. https://doi.org/10.1103/PhysRevB.100.014423 (2019).
45. Sharma, P. *et al.* Spin reorientation transition and spin dynamics study of perovskite orthoferrite $TmFeO_3$ detected by electron paramagnetic resonance. *Phys. Chem. Chem. Phys.* **22**, 21403–21411. https://doi.org/10.1039/D0CP00918K (2020).
46. Hou, L. *et al.* Spin-reorientation transition driven by double exchange in $CeFeO_3$ ceramics. *J. Phys. Chem. C* **124**, 15399–15405. https://doi.org/10.1021/acs.jpcc.0c00379 (2020).
47. Bonilla, C. M. *et al.* Universal behavior for magnetic entropy change in magnetocaloric materials: An analysis on the nature of phase transitions. *Phys. Rev. B* **81**, 224424. https://doi.org/10.1103/PhysRevB.81.224424 (2010).
48. Gilleo, M. A. Magnetic properties of a gadolinium orthoferrite, $GdFeO_3$. *Crystal. J. Chem. Phys.* **24**, 1239–1243. https://doi.org/10.1063/1.1742747 (1956).
49. Gorodetsky, G. & Treves, D. Second-order susceptibility terms in orthoferrites at room temperature. *Phys. Rev.* **135**, A97–A101. https://doi.org/10.1103/PhysRev.135.A97 (1964).
50. Mikami, I. Paramagnetic behavior of rare-earth ions in some orthoferrites. *J. Phy. Soc. Jpn* **34**, 338–342. https://doi.org/10.1143/JPSJ.34.338 (1973).
51. Ganeshraj, C., Pradheesh, R. & Santhosh, P. N. Structural, magnetic, transport and magnetocaloric properties of metamagnetic DyMn0.5Co0.5O3. *J. Appl. Phys.* **111**, 07A914. https://doi.org/10.1063/1.3672067 (2012).
52. Midya, A. *et al.* Magnetocaloric effect in $HoMnO_3$ crystal. *Appl. Phys. Lett.* **96**, 142514. https://doi.org/10.1063/1.3386541 (2010).
53. Palacios, E. *et al.* Effect of Gd polarization on the large magnetocaloric effect of $GdCrO_4$ in a broad temperature range. *Phys. Rev. B* **93**, 064420. https://doi.org/10.1103/PhysRevB.93.064420 (2016).
54. Midya, A., Khan, N., Bhoi, D. & Mandal, P. 3d–4f spin interaction induced giant magnetocaloric effect in zircon-type $DyCrO_4$ and $HoCrO_4$ compounds. *Appl. Phys. Lett.* **103**, 092402. https://doi.org/10.1063/1.4819768 (2013).
55. Ben Hassine, R. *et al.* Enhanced relative cooling power of Fe-doped La0.67Sr0.22Ba0.11Mn1-xFexO3 perovskites: Structural, magnetic and magnetocaloric properties. *J. Alloys Compd.* **649**, 996–1006. https://doi.org/10.1016/j.jallcom.2015.07.034 (2015).
56. Selmi, R., Chérif, W., Sarabando, A. R., Ferreira, N. M. & Ktari, L. Enhanced relative cooling power of lanthanum-deficiency manganites La0.77−xMg0.23MnO3 ($0 \le x \le 0.2$): Structural, magnetic and magnetocaloric properties. *J. Mater. Sci.: Mater. Electron.* **33**, 1703–1723 (2022).
57. Anwar, M. S., Ahmed, F. & Koo, B. H. Enhanced relative cooling power of Ni1−xZnxFe2O4 ($0.0 \leqslant x \leqslant 0.7$) ferrites. *Acta. Mater.* **71**, 100–107. https://doi.org/10.1016/j.actamat.2014.03.002 (2014).
58. Skini, R. *et al.* Large room temperature relative cooling power in La0.5Pr0.2Ca0.1Sr0.2MnO3. *J. Alloys Compd.* **827**, 154292 (2020).
59. Debnath, J. C., Zeng, R., Kim, J. H., Chen, D. P. & Dou, S. X. Anisotropic and excellent magnetocaloric properties of $La_{0.7}Ca_{0.3}MnO_3$ single crystal with anomalous magnetization. *Mater. Sci. Eng. B* **177**, 48–53. https://doi.org/10.1016/j.mseb.2011.09.034 (2012).
60. Balli, M. *et al.* On the magnetocaloric effect in the multiferroic hexagonal $DyMnO_3$ single crystals. *J. Magn. Magn. Mater.* **374**, 252–257. https://doi.org/10.1016/j.jmmm.2014.08.009 (2015).
61. Jia, J.-H. *et al.* Giant magnetocaloric effect in the antiferromagnet $GdScO_3$ single crystal. *J. Alloys Compd.* **803**, 992–997. https://doi.org/10.1016/j.jallcom.2019.06.361 (2019).
62. Sucksmith, W. & Thompson, J. E. (1954) The magnetic anisotropy of cobalt. *Proceedings of the Royal Society of London Series A. Mathematical and Physical Sciences* **225**, 362–375, https://doi.org/10.1098/rspa.1954.0209
63. Nikitin, S. A. *et al.* Magnetization, magnetic anisotropy and magnetocaloric effect of the $Tb_{0.2}Gd_{0.8}$ single crystal in high magnetic fields up to 1 T in region of a phase transition. *Acta. Mater.* **161**, 331–337. https://doi.org/10.1016/j.actamat.2018.09.017 (2018).

Acknowledgements

This work was supported by the National Research Foundation of Korea (NRF) through grants NRF-2017R1A5A1014862 (SRC program: vdWMRC center), NRF-2021R1A2C1006375, and NRF-2022R1A2C1006740. We would like to thank Editage (www.editage.co.kr) for English language editing.

Author contributions

N.L. and Y.J.C. conceived the project. H.J.S. synthesized the single crystals. H.J.S., J.S.K, and J.H.K. measured the physical properties of the crystals. H.J.S., N.L. and Y.J.C. analyzed the data and prepared the manuscript. K.W.J. estimated the energy of magnetic anisotropy. All the authors have read and approved the final version of the manuscript.

Competing interests

The authors declare no competing interests.

Additional information

Correspondence and requests for materials should be addressed to N.L. or Y.J.C.

Reprints and permissions information is available at www.nature.com/reprints.

Publisher's note Springer Nature remains neutral with regard to jurisdictional claims in published maps and institutional affiliations.

Open Access This article is licensed under a Creative Commons Attribution 4.0 International License, which permits use, sharing, adaptation, distribution and reproduction in any medium or format, as long as you give appropriate credit to the original author(s) and the source, provide a link to the Creative Commons licence, and indicate if changes were made. The images or other third party material in this article are included in the article's Creative Commons licence, unless indicated otherwise in a credit line to the material. If material is not included in the article's Creative Commons licence and your intended use is not permitted by statutory regulation or exceeds the permitted use, you will need to obtain permission directly from the copyright holder. To view a copy of this licence, visit http://creativecommons.org/licenses/by/4.0/.

© The Author(s) 2023